Letter

Correspondence between dynamic higher-order topological insulator and synthetic higher-order Dirac semimetal

Haonan Wang,[1] Hui Liu,[1,*] Yuanshuo Liu,[1] Yugan Tang,[1] Pengtao Lai,[1] Hua Cheng,[1,†] and Shuqi Chen[1,2,3,‡]

[1]*The Key Laboratory of Weak Light Nonlinear Photonics, Ministry of Education, School of Physics and TEDA Institute of Applied Physics, Nankai University, Tianjin 300071, China*

[2]*School of Materials Science and Engineering, Smart Sensing Interdisciplinary Science Center, Nankai University, Tianjin 300350, China*

[3]*The Collaborative Innovation Center of Extreme Optics, Shanxi University, Taiyuan, Shanxi 030006, China*

(Received 12 February 2025; accepted 14 May 2025; published 29 May 2025)

With the recent discovery of the correspondence between low-dimensional dynamical systems and high-dimensional topological insulators through the pumping process, many efforts have been made to generalize these correspondences to other topological phases. Yet, there is ongoing ambiguity about the correspondence of higher-order topological semimetals. Here, we propose a correspondence between a two-dimensional (2D) dynamic higher-order system and three-dimensional (3D) higher-order Dirac semimetals (HODSMs) through synthetic space consisting of a 2D lattice and a one-dimensional parameter dimension. We explore the evolution of the 2D higher-order topological insulator in a hexagonal acoustic crystal and find all the hallmarks of 3D HODSM in it, including Dirac points, surface states, and higher-order hinge states. By measuring the local density of states and acoustic pressure fields evolved in the 2D acoustic samples, we show that the system undergoes band gap-closing points, mapping to Dirac points in 3D synthetic space. The corner states evolving in nontrivial topological phase constitute hinge states connecting synthetic Dirac points. Our research deepens the understanding of the connections between different topological phases and may inspire further exploration of other topological effects in high-dimensional systems.

DOI: 10.1103/PhysRevB.111.L201408

Introduction. Higher-order topological insulators (HOTIs), as a new topological phase of matter that goes beyond the conventional bulk-boundary correspondence, have attracted a lot of attention in the last few years [1–5]. In general, an hth-order topological insulator in a d-dimensional system is characterized by $(d-h)$D boundary states with $h > 2$, different from conventional topological insulators with only $(d-1)$D boundary states. In addition to topological insulators, a higher-order topology can extend to topological semimetals with nontrivial higher-order topological states [6–10]. Compared with conventional topological semimetals that only host two-dimensional (2D) surface Fermi arcs, higher-order topological semimetals also host intriguing one-dimensional (1D) hinge states connecting projected Dirac points or Weyl points. Higher-order Dirac semimetals (HODSMs) can transition to higher-order nodal ring semimetals (HONRSMs) by breaking C_3 symmetry, and higher-order Weyl semimetals (HOWSMs) by breaking C_3 and mirror symmetries [11]. Thus, HODSMs have been an important bridge for investigating higher-order topological semimetals. Higher-order topological semimetals have been extensively studied in phononic crystals [12–19] and photonic crystals [20,21]. Classical wave systems have become an important platform for testing and implementing topological physics due to the high flexibility and controllability of wave trapping and manipulation [22–27].

In addition to static systems, similar topological states also exist in dynamical systems, such as Floquet systems [28] and topological pumpings [29]. In Floquet systems, periodic modulation can create an effective magnetic field, which breaks time-reversal symmetry and induces topologically protected one-way edge states [30,31]. Floquet systems provide a method to break time-reversal symmetry without applying external fields and connect the Chern topological phase with dynamically driven systems. By manipulating an adiabatic cycle of particles or topological states, 1D topological pumping is equivalent to the 2D integer quantum Hall effect [32], and 2D topological pumping corresponds to the four-dimensional integer quantum Hall effect characterized by the second Chern number [33]. Since a bridge has been established between low-dimensional insulators and high-dimensional quantum Hall effects, topological pumping is regarded as a tool for probing high-dimensional physics. It has been realized in various systems, including photonic waveguides, cold atoms, and acoustic systems [34–36]. More recently, the higher-order counterpart of topological pumping has been proposed and observed in photonic waveguide arrays, manifesting corner state transfer in the bulk band gap [37]. It is worth noting that this higher-order topological pumping corresponds to a three-dimensional (3D) second-order topological insulator with chiral hinge states, where the bulk band gap remains open during the pumping process. In addition to the high-order topological pumping described by the Chern number,

*Contact author: hliu@nankai.edu.cn
†Contact author: hcheng@nankai.edu.cn
‡Contact author: schen@nankai.edu.cn

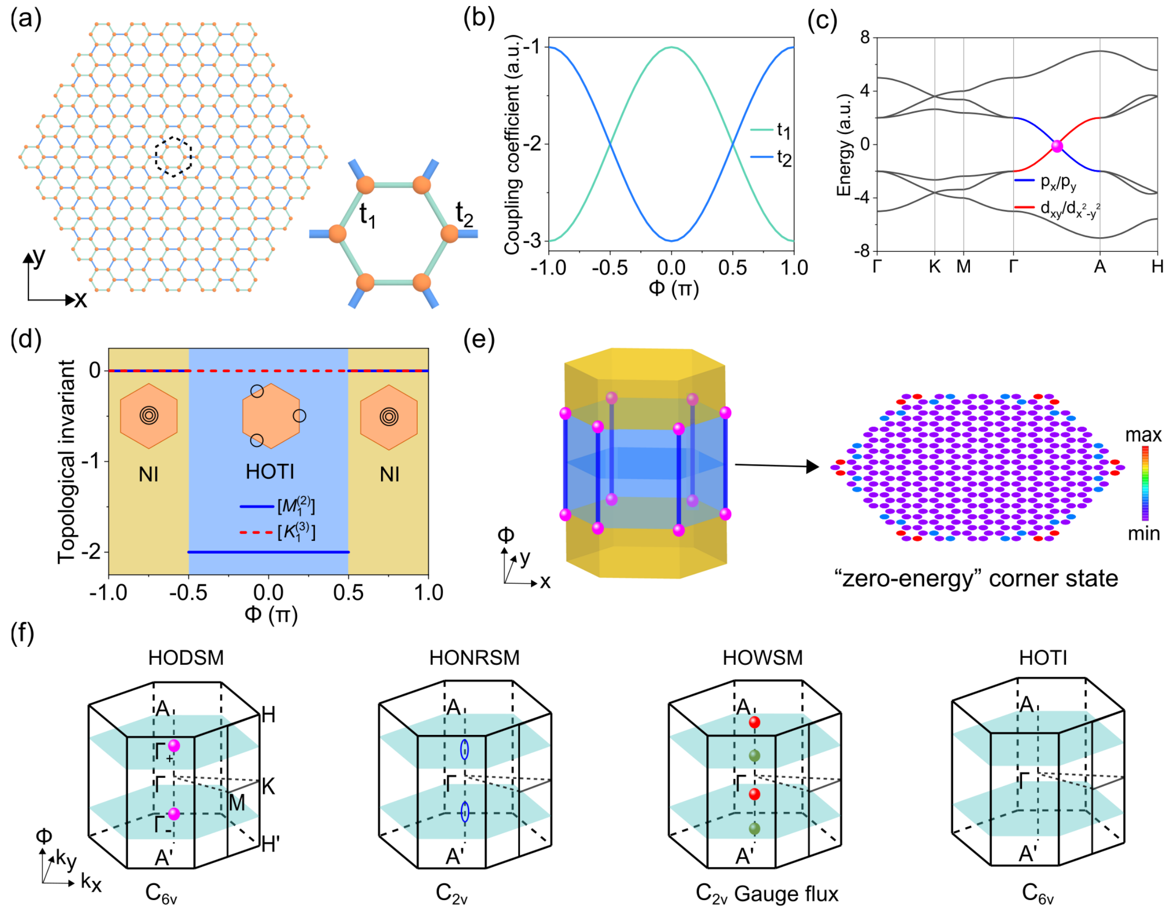

FIG. 1. Tight-binding model of the dynamic HOTI. (a) Schematic of the 2D hexagonal lattice model with modulated intracell coupling t_1 (green tubes) and intercell coupling t_2 (blue tubes). (b) Intra- and intercell coupling coefficients as functions of parameter ϕ. (c) Bulk band structures of the $H(k_x, k_y, \phi)$ along the high-symmetry lines. (d) Topological invariant $\chi^{(6)} = ([M_1^{(2)}], [K_1^{(3)}])$ along ϕ. Yellow and blue colors denote normal insulator (NI) and HOTI phases. (e) "Zero-energy" corner states of the 2D hexagonal model in the nontrivial phase (right panel) constitute the higher-order hinge states in the synthetic 3D space (left panel). (f) Brillouin zones of HONRSM, HOWSM, and 3D HOTI. Purple spheres: Dirac points. Blue rings: nodal rings. Red and green spheres: pairs of Weyl points.

researchers proposed a high-order topological pumping related to the boundary topology described by the boundary Chern number [38]. So far, the previous works mainly focus on the correspondence between dynamic low-dimensional topological insulators and high-dimensional topological insulators [34–39]. In these studies, the band gap remains open throughout the evolution process. A natural question arises: How does the relationship change if the band gap closes? Although the higher-order corner state transition in a closed band gap has been proposed as a HOWSM [40], the subtle connection between the dynamical evolution of low-dimensional HOTIs and high-dimensional higher-order semimetals has not been fully revealed and requires further investigation.

In this Letter, we proposed a correspondence between the evolution of 2D HOTI and 3D HODSM through synthetic dimensions. We built a 2D hexagonal acoustic crystal with parameter-modulated coupling and observed its evolution, which corresponds to a HODSM in 3D synthetic space (2D lattice and 1D parameter dimension). The 2D hexagonal acoustic crystal with given parameters along the parameter space is the 2D slices of the 3D HODSM, which can be classified into trivial and nontrivial higher-order topological phases described by the topological invariant $\chi^{(6)} = ([M_1^{(2)}], [K_1^{(3)}])$. The 2D system periodically undergoes the closing and reopening of the band gap as the parameters evolve, where the gap-closing points are fourfold linear degeneracies corresponding to the Dirac points. The corner states of the 2D hexagonal acoustic crystal with a nontrivial higher-order topological phase along the parameter space constitute the higher-order hinge states of the 3D HODSM. We experimentally measured the local density of states (LDOS) of the acoustic crystals along the parameter dimension, which clearly manifests the existence of the higher-order hinge states connecting the projected Dirac points. This research broadens the possibilities for controlling sound waves by presenting an exceedingly simple method for producing HODSMs in synthetic space.

Model and methods. We start from a 2D hexagonal tight-binding model with parameter-modulated intra- and intercell couplings, as shown in Fig. 1(a). For any fixed value of the parameter, the hexagonal model forms a 2D Kekulé lattice array with six atoms per unit cell, denoted by orange spheres. The intra- and intercell couplings, represented by blue and green tubes, are modulated as functions of $t_1(\phi) = t_0 + \delta\cos(\phi)$ and

$t_2(\phi) = t_0 - \delta\cos(\phi)$, respectively, over a period, where $t_0 = -2\delta = 1$, as shown in Fig. 1(b). The tight-binding Hamiltonian of a unit cell with parameter-modulated coupling terms can be described as

$$H(k_x, k_y, \phi) = \begin{pmatrix} 0 & h_{12} & 0 & h_{14} & 0 & h_{16} \\ h_{12}^* & 0 & h_{23} & 0 & h_{25} & 0 \\ 0 & h_{23}^* & 0 & h_{34} & 0 & h_{36} \\ h_{14}^* & 0 & h_{34}^* & 0 & h_{45} & 0 \\ 0 & h_{25}^* & 0 & h_{45}^* & 0 & h_{56} \\ h_{16}^* & 0 & h_{36}^* & 0 & h_{56}^* & 0 \end{pmatrix}, \quad (1)$$

where $h_{12} = h_{23} = h_{34} = h_{45} = h_{56} = h_{16} = t_1(\phi)$, $h_{14} = t_2(\phi)e^{i(\frac{k_x}{2}+\frac{\sqrt{3}k_y}{2})}$, $h_{25} = t_2(\phi)e^{i(-\frac{k_x}{2}+\frac{\sqrt{3}k_y}{2})}$, $h_{36} = t_2(\phi)e^{-ik_x}$, and the lattice constant is set to 1 for simplicity. When the lattice plane (x and y dimension) together with the parameter axis are considered as a 3D synthetic space, one can find a pair of fourfold linear degenerate points located at $(0, 0, \pm 0.5\pi)$. The fourfold linear degenerate points created by band inversion are located at the critical points where the intra- and intercell coupling strengths are equal. Near each fourfold degeneracy, there are two doubly degenerate states, dipolar states p_x/p_y represented by blue lines and quadrupolar states $d_{xy}/d_{x^2-y^2}$ represented by red lines, as plotted in Fig. 1(c). The doubly degenerate states can be hybridized to $p_\pm = p_x \pm ip_y$ and $d_\pm = d_{xy} \pm id_{x^2-y^2}$ states with pseudospin up and pseudospin down. Based on $k \cdot p$ perturbation theory, the effective Hamiltonian near the degenerate points in the basis $(p_x + ip_y, d_{xy} + id_{x^2-y^2}, p_x - ip_y, d_{xy} - id_{x^2-y^2})^T$ can be obtained in block-diagonal form as

$$H_{\text{eff}}(k_x, k_y, \phi) = \begin{pmatrix} h(k_x, k_y, \phi) & 0 \\ 0 & h^*(-k_x, -k_y, -\phi) \end{pmatrix}, \quad (2)$$

where $h(k_x, k_y, \phi) = \begin{pmatrix} 2\delta\cos(\phi) & A(k_x - ik_y) \\ A^*(k_x + ik_y) & -2\delta\cos(\phi) \end{pmatrix}$ and $A = (-i + \sqrt{3})[t_0 - \delta\cos(\phi)]/4$. The tight-binding Hamiltonian analysis is available in Supplemental Material Sec. I [41]. The effective Hamiltonian has a form similar to the minimal 4×4 Hamiltonian of a Dirac semimetal [42], which indicates that the parameter-modulated hexagonal model in 3D synthetic space is equivalent to a Dirac semimetal. The pair of fourfold linear degenerate points on the planes $\phi = \pm 0.5\pi$ are actually Dirac points with a nontrivial topological charge of $Z_2 = 1$. The details for topological charge can be found in Supplemental Material Sec. II [41].

For different slice of ϕ, the higher-order topological properties of the parameter-modulated 2D hexagonal model with chiral and C_{6v} symmetries can be characterized by the topological invariant $\chi^{(6)} = ([M_1^{(2)}], [K_1^{(3)}])$ and the secondary topological index $Q_{\text{corner}}^{(6)} = \frac{e}{4}[M_1^{(2)}] + \frac{e}{6}[K_1^{(3)}] \mod e$ [43,44]. $[M_1^{(2)}] = \#M_1^{(2)} - \#\Gamma_1^2$ and $[\mathrm{K}_1^{(3)}] = \#K_1^{(3)} - \#\Gamma_1^3$ are C_2 and C_3 topological invariants, respectively. Here, $\#\Pi_1^{(n)}$ is the number of states below the gap with C_n-rotational eigenstates $+1$ at the Π point of the Brillouin zone. Since the C_3 symmetry commutes with the chiral symmetry, there is $[K_1^{(3)}] = 0$ for all values of ϕ. In contrast, C_2 symmetry and chiral symmetry are not commutative, and the topological invariant $[M_1^{(2)}]$ is not always zero. The topological invariant $[M_1^{(2)}] = -2$ indicates a nontrivial higher-order topology in the range of $\phi \in (-0.5\pi, 0.5\pi)$, while the topological invariant $[M_1^{(2)}] = 0$ indicates a trivial one, as shown in Fig. 1(d). There are topological phase transitions between the topologically trivial and nontrivial phase at $\phi = \pm 0.5\pi$, mapping to the Dirac points with closed band gaps. Wannier centers are located at the center of the unit cell in the higher-order topologically trivial phase, but at the boundaries in the nontrivial phase, as shown in the inset of Fig. 1(d). The existence of topological corner states depends not only on the global topological properties of the bulk but also on the shapes of the finite-size models. The details are presented in Supplemental Material Sec. III [41]. We use a finite-size hexagonal model of side length $5a$, featuring six obtuse-angled corners with topological index $N = 1$, to investigate the higher-order topological properties. The chiral-symmetry-protected "zero-energy" corner states with $Q_{\text{corner}}^{(6)} = \frac{e}{2}$ of the finite-size hexagonal model appear in the topologically nontrivial ranges, while they disappear in the trivial ones, as depicted in the right panel of Fig. 1(e). From the perspective of 3D synthetic space, the "zero-energy" corner states in the topologically nontrivial range constitute the higher-order hinge states of the HODSM (blue lines), connecting a pair of projected Dirac points (purple spheres), as shown in the left panel of Fig. 1(e).

As a central gapless topological phase, the HODSM in 3D synthetic space can transition to other higher-order topological phases, such as HONRSM, HOWSM, and 3D HOTI, by breaking the symmetry or precisely adjusting the coupling strength, as shown in Fig. 1(f). When reducing the C_{6v} symmetry to C_{2v} symmetry by adding an on-site potential in some atoms, the Dirac point denoted by the purple sphere can be split into a nodal ring (blue ring). When further introducing a synthetic gauge flux by adding complex coupling into the intracell coupling, the nodal ring degeneracy can be opened as a pair of Weyl points with topological charge $C = 1$ and $C = -1$ denoted by green and red spheres, respectively. When the intra- and intercell couplings are precisely adjusted to $t_1(\phi) < t_2(\phi)$, the HODSM transitions into a 3D HOTI. The details are provided in Supplemental Material Sec. IV [41]. Since HODSM is an ancestor model for the other higher-order phases, we focus on its acoustic realization and observation.

In accordance with the above scenario, we employ a hexagonal acoustic crystal to implement the 2D dynamic system. The hexagonal unit cell with a lattice constant $a = 66.9$ mm is illustrated in Fig. 2(a), which contains six acoustic resonators connected by parameter-modulated intra- and intercell cylinder tubes. Each resonator, as an artificial atom, has a radius and height of $r_0 = 6.8$ mm and $H = 20.4$ mm, respectively, denoted by orange cylinders. The green and blue tubes, connecting the resonators at heights $H/4$ and $3H/4$, provide the intra- and intercell couplings, respectively. The strengths of the intracell and intercell couplings are controlled by the radius of tubes $r_1(\phi) = r_0 - \delta\cos(\phi)$ and $r_2(\phi) = r_0 + \delta\cos(\phi)$, respectively, where $r_0 = 2.975$ mm and $\delta = 1.275$ mm. The simulated bulk band structures along the high-symmetry lines are shown in Fig. 2(b), where a Dirac point with a fourfold linear band crossing can be found in the synthetic space. There are a pair of twofold degenerate bands along the ΓA direction due to the 2D irreducible representation of C_{3v} symmetry. A Dirac point formed by the two twofold degenerate bands crossing at $(0, 0, 0.5\pi)$

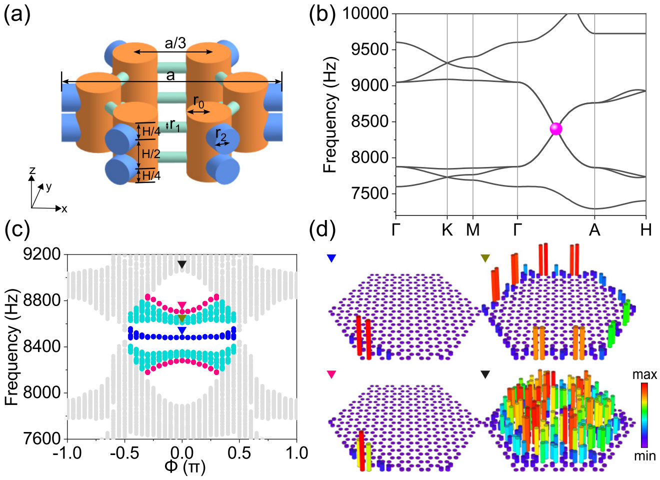

FIG. 2. Acoustic implementation of the dynamic 2D HOTI. (a) Unit cell of the parameter-modulated acoustic crystal. (b) Bulk band structures of the hexagonal acoustic crystal along the high-symmetry lines. (c) Projected band dispersions of a finite hexagonal acoustic crystal. (d) Acoustic pressure fields for the topological corner states, edge states, trivial corner states, and bulk states of the parameter-modulated HOTI at $\phi = 0$.

is denoted by a purple sphere. Then, we construct a finite hexagonal structure with side length $L = 5a$ and calculate the projected band dispersions along the parameter ϕ, as shown in Fig. 2(c). The topological corner states, arising from the higher-order nontrivial topological phase in the range of $\phi \in (-0.5\pi, 0.5\pi)$, are represented by blue dots. Along the parameter ϕ, topological corner states appear and disappear with the gap closure and reopening. In addition to the "zero-energy" topological corner states, there are two pairs of nonhybridized homogeneous trivial corner states and edge states distributed symmetrically above and below the frequency of the topological corner states. Due to topological protection, the eigenfrequencies of the topological corner states are not affected by small disorder in the hexagonal acoustic crystal, while the trivial ones lack such robustness. When disorder is introduced in the bulk and edge cavities, the topological corner states at 8485 Hz are almost unaffected by small disorder, but the trivial corner states are more susceptible to disorder, as discussed in Supplemental Material Sec. V [41]. For a given parameter $\phi = 0$, the acoustic eigenpressure fields present some typical modes of the parameter-modulated 2D HOTI, including topological corner states, trivial corner states, edge states, and bulk states, as shown in Fig. 2(d). There are six topological corner states distributed at six different corners due to C_6 symmetry. Only one of the corner states is presented here. The pressure fields clearly distinguish the topological corner state and trivial corner state. The former is primarily concentrated in two resonators near one corner, while the latter is mainly concentrated in three resonators. The fields of edge and bulk states are primarily located at the edge and bulk resonators, respectively, and have little spatial overlap with the corner resonators. If the parameter axis ϕ is viewed as a synthetic dimension, the evolution of the 2D finite structure can be understood through higher-order semimetal physics. Topological phase transition points at $(0, 0, \pm 0.5\pi)$ form a fourfold linear band crossing, i.e., the Dirac points, in 3D synthetic space. The hinge states, constituted by corner states in the topologically nontrivial phase range $\phi \in (-0.5\pi, 0.5\pi)$, connect the Dirac points along the parameter axis. All the hallmarks of HODSMs, such as Dirac points, surface states, topological, and trivial hinge states, can be found in this 2D parameter-modulated system, corresponding to topological phase transition points, the evolution of edge states (green dots), topological corner states (blue dots), and trivial corner states (red dots), respectively.

Observation of the dynamic 2D HOTI corresponding to a HODSM. To confirm the correspondence between the 2D dynamic HOTI and 3D HODSM, we observed the evolution of the parameter-modulated HOTI and mapped it to a 3D semimetal system in experiments. We fabricated a series of acoustic hexagonal samples with a side length $L = 5a$ using 3D printing technology, where the parameter ϕ is discretized at an interval of 0.1π to mimic the evolution [45–48]. The parameter-modulated HOTI can approach the ideal continuous evolution when the sample discretization is infinitely small. Discretization usually does not become infinitesimal due to experimental limitations, but it is sufficient for mimicking the key features of the evolution process. One of the samples with $\phi = 0$ is shown in Fig. 3(a), where the inset presents the details of one corner. Small holes are left at the top and bottom of each resonator for measurement purposes. These holes are blocked with plugs when not in use to maintain the integrity of the resonator. While a balanced armature speaker was placed at the bottom of one resonator to excite the sound field, a microphone was placed at the top of the same resonator to detect the acoustic signal. For each acoustic sample with different evolved values ϕ, the LDOS can be extracted from the local pressure response of each resonator (the details for LDOS can be found in Supplemental Material Sec. VI [41]). By measuring the LDOS of several acoustic hexagonal samples with different values ϕ, we obtained the projected band dispersions of the 2D evolved HOTI, as shown in Fig. 3(b). Through full-wave simulation, simulated projected band dispersions can be extracted from the LDOS using the same technique as the experiments, as plotted in Fig. 3(c). The measured projected band dispersions match well with the simulated results. Since the intra- and intercell couplings modulated by cosine functions are symmetric about $\phi = 0$, the projected band structures are also symmetric about $\phi = 0$. The results of projected band dispersions reveal two gap-closing points located at $\phi = \pm 0.5\pi$, which distinguish the two distinct topological phases: The topologically trivial one is distributed at $|\phi| > 0.5\pi$, while the nontrivial one is distributed at $\phi \in (-0.5\pi, 0.5\pi)$. In the 2D evolved acoustic system, the topologically protected corner states exist in the range of a topologically nontrivial phase at 8485 Hz and form topological hinge states in the synthetic 3D space. The corresponding measured 2D acoustic pressure fields at 8485 Hz in different planes $\phi \in [0, 0.5\pi]$, representing slices of topological hinge states in the synthetic 3D space, are given in Fig. 3(d). All the corner eigenstates are simultaneously excited, resulting in a symmetrical distribution of the sound pressure field at each corner. Since the gap closure points correspond to the Dirac points that connect the topological hinge states, the slices of the hinge state near $\phi = 0.5\pi$ mix with the surface and bulk states. The other slices show that

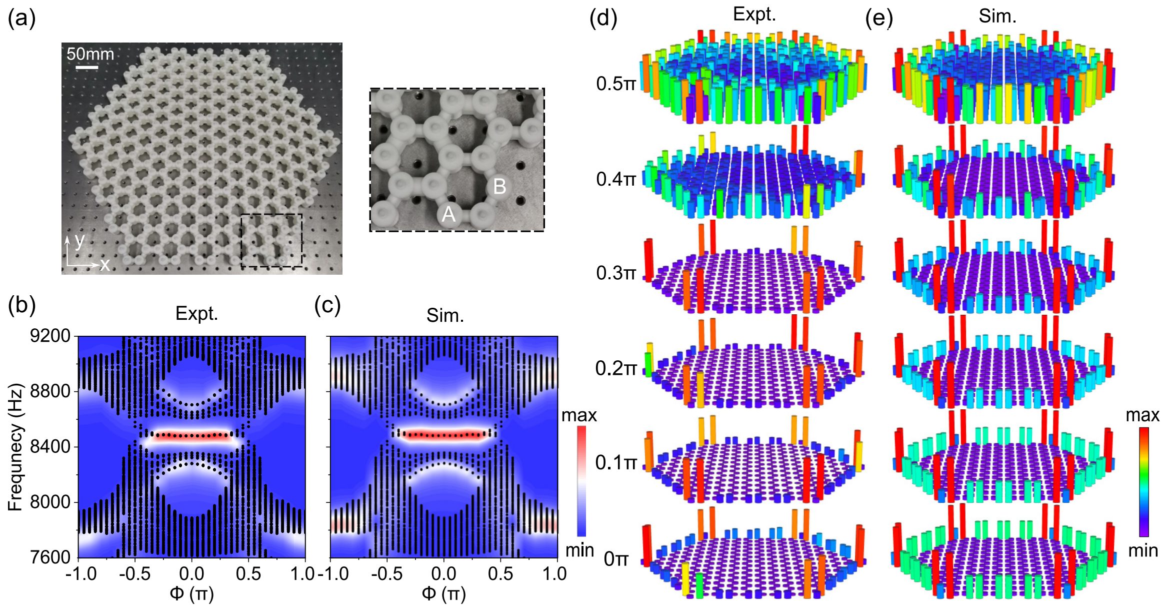

FIG. 3. Observation of the parameter-modulated 2D HOTI corresponding to a HODSM. (a) Photograph of the sample with $\phi = 0$. (b), (c) Experimentally measured projected band dispersions and simulated results by full-wave simulation, respectively. Color maps are results extracted from the experimental and simulated LDOS. Black dots are theoretical projected band dispersions. (d), (e) Measured and simulated 2D acoustic pressure fields at 8485 Hz show the existence of the topological hinge states and degenerate points, respectively.

topological hinge modes are mainly distributed in the A and B resonators along the parameter axis ϕ. The measured slices of the topological hinge modes are in good agreement with the simulated results, as displayed in Fig. 3(e). Experimental and theoretical evidence clearly shows that the evolution of the 2D HOTI corresponds to a 3D HODSM in synthetic space.

The correspondence between the evolution of low-dimensional systems and high-dimensional systems not only offers a unique perspective for the study of topological semimetals, but also provides a method for investigating elusive high-dimensional topological physics. In higher dimensions, topological systems will exhibit more exotic and rich topological properties, such as a 3D Chern insulator with torus loops and links characterized by the vector Chern number [49], a four- and six-dimensional quantum Hall effect characterized by the second and third Chern number [50,51], and a five-dimensional Weyl semimetal with a Yang monopole and linked Weyl surfaces [52,53]. Due to the limitations of real-space dimensions, it is difficult to directly realize the high-dimensional topological phenomena beyond three dimensions but can be investigated in low-dimensional dynamical systems. The four- and six-dimensional quantum Hall effects are equivalent to 2D and 3D pumping in low-dimensional systems [34,35,51], respectively. By combining space and time dimensions, researchers recently proposed a new topological phase beyond the Floquet paradigm in $(D+1)$-dimensional space-time crystals [54] and successfully simulated the Fermi-arc surface state of the space-time Weyl semimetal in $(3+1)$-dimensional circuits [55]. Future research can explore more novel physical properties and applications of high-dimensional topological systems via low-dimensional dynamical systems.

Conclusions. In summary, we have established a bridge between 2D HOTI and 3D HODSM through synthetic dimensions. We demonstrated that a phononic crystal, designed as a parameter-modulated hexagonal lattice, exhibits all the signatures of the 3D HODSM, including Dirac points, surface states, and hinge states. We observed that the corner states, the hallmark of HOTI, exist in the topologically nontrivial phase range between two gap-closing points along the parameter axis, which map to the higher-order hinge states connecting Dirac points in a HODSM. This approach can be extended to higher dimensions to explore more topological phenomena, and generalized to other physical systems, such as mechanical systems, photonic crystals, and electric circuits.

Acknowledgments. This work was supported by the National Key Research and Development Program of China (Grant No. 2022YFA1404501), the National Natural Science Foundation of China (Grants No. 12304486, No. 12474331, No. 123B2069, No. 12192253, and No. W2441005), and the Natural Science Foundation of Tianjin for Distinguished Young Scientists (Grants No. 22JCZDJC00400 and No. 23JCQNJC01450).

Data availability. The data that support the findings of this article are not publicly available. The data are available from the authors upon reasonable request.

[1] W. A. Benalcazar, B. A. Bernevig, and T. L. Hughes, Quantized electric multipole insulators, Science **357**, 61 (2017).

[2] W. A. Benalcazar, B. A. Bernevig, and T. L. Hughes, Electric multipole moments, topological multipole moment pumping,

and chiral hinge states in crystalline insulators, Phys. Rev. B **96**, 245115 (2017).
[3] F. Schindler, A. M. Cook, M. G. Vergniory, Z. Wang, S. S. P. Parkin, B. A. Bernevig, and T. Neupert, Higher-order topological insulators, Sci. Adv. **4**, eaat0346 (2018).
[4] B. Xie, H.-X. Wang, X. Zhang, P. Zhan, J.-H. Jiang, M. Lu, and Y. Chen, Higher-order band topology, Nat. Rev. Phys. **3**, 520 (2021).
[5] F. Schindler, Z. Wang, M. G. Vergniory, A. M. Cook, A. Murani, S. Sengupta, A. Y. Kasumov, R. Deblock, S. Jeon, I. Drozdov *et al.*, Higher-order topology in bismuth, Nat. Phys. **14**, 918 (2018).
[6] M. Ezawa, Higher-order topological insulators and semimetals on the breathing kagome and pyrochlore lattices, Phys. Rev. Lett. **120**, 026801 (2018).
[7] M. Lin and T. L. Hughes, Topological quadrupolar semimetals, Phys. Rev. B **98**, 241103(R) (2018).
[8] H.-X. Wang, Z.-K. Lin, B. Jiang, G.-Y. Guo, and J.-H. Jiang, Higher-order Weyl semimetals, Phys. Rev. Lett. **125**, 146401 (2020).
[9] S. A. A. Ghorashi, T. Li, and T. L. Hughes, Higher-order Weyl semimetals, Phys. Rev. Lett. **125**, 266804 (2020).
[10] B. J. Wieder, Z. Wang, J. Cano, Xi Dai, L. M. Schoop, B. Bradlyn, and B. A. Bernevig, Strong and fragile topological Dirac semimetals with higher-order Fermi arcs, Nat. Commun. **11**, 627 (2020).
[11] H. Qiu, M. Xiao, F. Zhang, and C. Qiu, Higher-order Dirac sonic crystals, Phys. Rev. Lett. **127**, 146601 (2021).
[12] L. Luo, H.-X. Wang, Z.-K. Lin, B. Jiang, Y. Wu, F. Li, and J.-H. Jiang, Observation of a phononic higher-order Weyl semimetal, Nat. Mater. **20**, 794 (2021).
[13] Q. Wei, X. Zhang, W. Deng, J. Lu, X. Huang, M. Yan, G. Chen, Z. Liu, and S. Jia, Higher-order topological semimetal in acoustic crystals, Nat. Mater. **20**, 812 (2021).
[14] C.-H. Xia, H.-S. Lai, X.-C. Sun, C. He, and Y.-F. Chen, Experimental demonstration of bulk-hinge correspondence in a three-dimensional topological Dirac acoustic crystal, Phys. Rev. Lett. **128**, 115701 (2022).
[15] L. Yang, Y. Wang, Y. Meng, Z. Zhu, X. Xi, B. Yan, S. Lin, J. Chen, B.-j. Shi, Y. Ge, S.-Q. Yuan, H. Chen, H.-X. Sun, G.-G. Liu, Y. Yan, and Z. Gao, Observation of Dirac hierarchy in three-dimensional acoustic topological insulators, Phys. Rev. Lett. **129**, 125502 (2022).
[16] Q. Ma, Z. Pu, L. Ye, J. Lu, X. Huang, M. Ke, H. He, W. Deng, and Z. Liu, Observation of higher-order nodal-line semimetal in phononic crystals, Phys. Rev. Lett. **132**, 066601 (2024).
[17] H. Qiu, Y. Li, Q. Zhang, and C. Qiu, Discovery of higher-order nodal surface semimetals, Phys. Rev. Lett. **132**, 186601 (2024).
[18] Z. Pu, H. He, L. Luo, Q. Ma, L. Ye, M. Ke, and Z. Liu, Acoustic higher-order Weyl semimetal with bound hinge states in the continuum, Phys. Rev. Lett. **130**, 116103 (2023).
[19] L. Ye, Q. Wang, Z. Fu, H. He, X. Huang, M. Ke, J. Lu, W. Deng, and Z. Liu, Hinge modes of surface arcs in a synthetic Weyl phononic crystal, Phys. Rev. Lett. **133**, 126602 (2024).
[20] Z. Wang, D. Liu, H. T. Teo, Q. Wang, H. Xue, and B. Zhang, Higher-order Dirac semimetal in a photonic crystal, Phys. Rev. B **105**, L060101 (2022).
[21] Y. Pan, C. Cui, Q. Chen, F. Chen, Li Zhang, Y. Ren, N. Han, W. Li, X. Li, Z.-M. Yu *et al.*, Real higher-order Weyl photonic crystal, Nat. Commun. **14**, 6636 (2023).
[22] L. Lu, J. D. Joannopoulos, and M. Soljačić, Topological photonics, Nat. Photon. **8**, 821 (2014).
[23] G. Ma, M. Xiao, and C. T. Chan, Topological phases in acoustic and mechanical systems, Nat. Rev. Phys. **1**, 281 (2019).
[24] H. Xue, Y. Yang, and B. Zhang, Topological acoustics, Nat. Rev. Mater. **7**, 974 (2022).
[25] X. Zhang, F. Zangeneh-Nejad, Z.-G. Chen, M.-H. Lu, and J. Christensen, A second wave of topological phenomena in photonics and acoustics, Nature (London) **618**, 687 (2023).
[26] H. Wu, H. He, L. Ye, J. Lu, M. Ke, W. Deng, and Z. Liu, Acoustic valley filter, valve, and diverter, Adv. Mater. **37**, 2500757 (2025).
[27] Y. Hu, J. Wu, P. Ye, W. Deng, J. Lu, X. Huang, Ziyu Wang, M. Ke, and Z. Liu, Acoustic Exceptional line semimetal, Phys. Rev. Lett. **134**, 116606 (2025).
[28] S. Yin, E. Galiffi, and A. Alù, Floquet metamaterials, eLight **2**, 8 (2022).
[29] R. Citro and M. Aidelsburger, Thouless pumping and topology, Nat. Rev. Phys. **5**, 87 (2023).
[30] M. C. Rechtsman, J. M. Zeuner, Y. Plotnik, Y. Lumer, D. Podolsky, F. Dreisow, S. Nolte, M. Segev, and A. Szameit, Photonic Floquet topological insulators, Nature (London) **496**, 196 (2013).
[31] R. Fleury, A. B. Khanikaev, and A. Alu, Floquet topological insulators for sound, Nat. Commun. **7**, 11744 (2016).
[32] D. J. Thouless, Quantization of particle transport, Phys. Rev. B **27**, 6083 (1983).
[33] I. Petrides and O. Zilberberg, Higher-order topological insulators, topological pumps and the quantum Hall effect in high dimensions, Phys. Rev. Res. **2**, 022049(R) (2020).
[34] O. Zilberberg, S. Huang, J. Guglielmon, M. Wang, K. P. Chen, Y. E. Kraus, and M. C. Rechtsman, Photonic topological boundary pumping as a probe of 4D quantum Hall physics, Nature (London) **553**, 59 (2018).
[35] M. Lohse, C. Schweizer, H. M. Price, O. Zilberberg, and I. Bloch, Exploring 4D quantum Hall physics with a 2D topological charge pump, Nature (London) **553**, 55 (2018).
[36] H. Chen, H. Zhang, Q. Wu, Yu Huang, H. Nguyen, E. Prodan, X. Zhou, and G. Huang, Creating synthetic spaces for higher-order topological sound transport, Nat. Commun. **12**, 5028 (2021).
[37] W. A. Benalcazar, J. Noh, M. Wang, S. Huang, K. P. Chen, and M. C. Rechtsman, Higher-order topological pumping and its observation in photonic lattices, Phys. Rev. B **105**, 195129 (2022).
[38] Z. Wang, L. Ye, Z. Pu, Q. Ma, H. He, J. Lu, W. Deng, X. Huang, M. Ke, and Z. Liu, Higher-order topological transport protected by boundary Chern number in phononic crystals, Commun. Phys. **7**, 193 (2024).
[39] J. F. Wienand, F. Horn, M. Aidelsburger, J. Bibo, and F. Grusdt, Thouless pumps and bulk-boundary correspondence in higher-order symmetry-protected topological phases, Phys. Rev. Lett. **128**, 246602 (2022).
[40] H. Liu, H. Wang, B. Xie, H. Cheng, Z. Liu, and S. Chen, Acoustic corner state transfer mapping to synthetic higher-order topological semimetal, Phys. Rev. B **108**, L161104 (2023).
[41] See Supplemental Material at http://link.aps.org/supplemental/10.1103/PhysRevB.111.L201408 for (i) tight-binding Hamiltonian, (ii) topological charge of the degeneracy, (iii) corner states at acute and obtuse-angled corners, (iv) different higher-order

topological phases transformed from HODSM, (v) robustness of the higher-order hinge states, and (vi) experimental measurements, LDOS, and numerical simulations, which includes Refs. [56–59].

[42] B.-J. Yang and N. Nagaosa, Classification of stable three-dimensional Dirac semimetals with nontrivial topology, Nat. Commun. **5**, 4898 (2014).

[43] J. Noh, W. A. Benalcazar, S. Huang, M. J. Collins, K. P. Chen, T. L. Hughes, and M. C. Rechtsman, Topological protection of photonic mid-gap defect modes, Nat. Photon. **12**, 408 (2018).

[44] W. A. Benalcazar, T. Li, and T. L. Hughes, Quantization of fractional corner charge in C_n-symmetric higher-order topological crystalline insulators, Phys. Rev. B **99**, 245151 (2019).

[45] T. Xia, Y. Li, Q. Zhang, X. Fan, M. Xiao, and C. Qiu, Observation of hybrid-order topological pump in a Kekulé-textured graphene lattice, Phys. Rev. B **108**, 125125 (2023).

[46] X. Ni, K. Chen, M. Weiner, D. J. Apigo, C. Prodan, A. Alu, E. Prodan, and A. B. Khanikaev, Observation of Hofstadter butterfly and topological edge states in reconfigurable quasi-periodic acoustic crystals, Commun. Phys. **2**, 55 (2019).

[47] Y.-X. Shen, L.-S. Zeng, Z.-G. Geng, D.-G. Zhao, Y.-G. Peng, and X.-F. Zhu, Acoustic adiabatic propagation based on topological pumping in a coupled multicavity chain lattice, Phys. Rev. Appl. **14**, 014043 (2020).

[48] L.-S. Zeng, Y.-X. Shen, Y.-G. Peng, D.-G. Zhao, and X.-F. Zhu, Selective topological pumping for robust, efficient, and asymmetric sound energy transfer in a dynamically coupled cavity chain, Phys. Rev. Appl. **15**, 064018 (2021).

[49] G.-G. Liu, Z. Gao, Q. Wang, X. Xi, Y.-H. Hu, M. Wang, C. Liu, X. Lin, L. Deng, S. A. Yang *et al.*, Topological Chern vectors in three-dimensional photonic crystals, Nature (London) **609**, 925 (2022).

[50] S.-C. Zhang and J. Hu, A four-dimensional generalization of the quantum Hall effect, Science **294**, 823 (2001).

[51] I. Petrides, H. M. Price, and O. Zilberberg, Six-dimensional quantum Hall effect and three-dimensional topological pumps, Phys. Rev. B **98**, 125431 (2018).

[52] S. Ma, Y. Bi, Q. Guo, B. Yang, O. You, J. Feng, Hong-Bo Sun, and S. Zhang, Linked Weyl surfaces and Weyl arcs in photonic metamaterials, Science **373**, 572 (2021).

[53] S. Ma, H. Jia, Y. Bi, S. Ning, F. Guan, H. Liu, C. Wang, and S. Zhang, Gauge field induced chiral zero mode in five-dimensional Yang monopole metamaterials, Phys. Rev. Lett. **130**, 243801 (2023).

[54] Y. Peng, Topological space-time crystal, Phys. Rev. Lett. **128**, 186802 (2022).

[55] W. Zhang, W. Cao, L. Qian, H. Yuan, and X. Zhang, Topolectrical space-times circuits, Nat. Commun. **16**, 198 (2025).

[56] R. Yu, X. L. Qi, A. Bernevig, Z. Fang, and X. Dai, Equivalent expression of $\mathbb{Z}_2$ topological invariant for band insulators using the non-Abelian Berry connection, Phys. Rev. B **84**, 075119 (2011).

[57] B. Xie, H. Liu, H. Cheng, Z. Liu, J. Tian, and S. Chen, Dirac points and the transition towards Weyl points in three-dimensional sonic crystals, Light: Sci. Appl. **9**, 201 (2020).

[58] J. C. Y. Teo and C. L. Kane, Topological defects and gapless modes in insulators and superconductors, Phys. Rev. B **82**, 115441 (2010).

[59] X. Ni, M. Weiner, A. Alu, and A. B. Khanikaev, Observation of higher-order topological acoustic states protected by generalized chiral symmetry, Nat. Mater. **18**, 113 (2019).